

Unmixing chromophores in human skin with a 3D multispectral optoacoustic mesoscopy system

Mathias Schwarz^{a,b}, Juan Aguirre^{a,b}, Dominik Soliman^{a,b}, Andreas Buehler^{a,b}, and Vasilis Ntziachristos^{a,b,+}

^aChair for Biological Imaging, Technische Universität München, Ismaningerstr. 22, 81675, München, Germany

^bInstitute for Biological and Medical Imaging, Helmholtz Zentrum München, Ingolstädter Landstr. 1, 85764, Neuherberg, Germany

+Corresponding author: v.ntziachristos@tum.de

ABSTRACT

The absorption of visible light by human skin is governed by a number of natural chromophores: Eumelanin, pheomelanin, oxyhemoglobin, and deoxyhemoglobin are the major absorbers in the visible range in cutaneous tissue. Label-free quantification of these tissue chromophores is an important step of optoacoustic (photoacoustic) imaging towards clinical application, since it provides relevant information in diseases. In tumor cells, for instance, there are metabolic changes (Warburg effect) compared to healthy cells, leading to changes in oxygenation in the environment of tumors. In malignant melanoma changes in the absorption spectrum have been observed compared to the spectrum of nonmalignant nevi. So far, optoacoustic imaging has been applied to human skin mostly in single-wavelength mode, providing anatomical information but no functional information. In this work, we excited the tissue by a tunable laser source in the spectral range from 413-680 nm with a repetition rate of 50 Hz. The laser was operated in wavelength-sweep mode emitting consecutive pulses at various wavelengths that allowed for automatic co-registration of the multispectral datasets. The multispectral raster-scan optoacoustic mesoscopy (MSOM) system provides a lateral resolution of $<60 \mu\text{m}$ independent of wavelength. Based on the known absorption spectra of melanin, oxyhemoglobin, and deoxyhemoglobin, three-dimensional absorption maps of all three absorbers were calculated from the multispectral dataset.

Keywords: Dermatology; Medical and biological imaging; Multispectral imaging; Photoacoustic imaging; Optoacoustic imaging

1. INTRODUCTION

Optoacoustic (photoacoustic) tomography allows for the detection of intrinsic or extrinsically administered molecules [1], e.g. melanin, oxyhemoglobin, and deoxyhemoglobin [2, 3], visualizing tumor hypoxia [4], or kidney perfusion [5]. Given this spectral ability, human skin is a well-suited target for multispectral raster-scan optoacoustic mesoscopy (MSOM) since its thickness varies from 1.5 mm to 4 mm, it is easily accessible, and contains numerous natural chromophores. The absorption of visible light by human skin is governed by the natural chromophores eumelanin, pheomelanin, oxyhemoglobin, doxyhemoglobin, bilirubin, and β -carotene. [6-9].

The quantification of tissue chromophores has great potential in the diagnosis and therapy of skin diseases. There are whole books on the impact of changes in oxygen saturation in the microenvironment of the tumor and new opportunities for cancer therapy arising thereof [10, 11]. It was shown that two hypoxia-inducible factors play a critical role in the progression of melanoma [12]. But hypoxia is not only found in skin cancer. For instance, hypoxia was observed in systemic sclerosis [13], and oxygen levels in ischemic wounds play an important role in the healing process [14].

For MSOM to work robustly, it is important that the set of multi-wavelength images is acquired from the same tissue volume, i.e. having the tissue at the same position, orientation and at the same morphological and physiological state throughout the wavelength scanning process. However, since MSOM is a high resolution modality even moderate motion of the subject during image acquisition may compromise the accuracy of the imaging result and there is always

likely to be motion when imaging live subjects. To date, no optoacoustic imaging group has been able to calculate 3D absorption maps of oxygen saturation, and melanin of the human skin, due to a lack of appropriate fast-tunable lasers.

Early optoacoustic imaging of human skin were acquired by a functional photoacoustic microscopy (fPAM) system, utilizing a laser with 10 Hz pulse repetition frequency (PRF). However, with fPAM blood oxygenation and melanin content have never been visualized in human skin [15]. With an adapted fPAM system based on a 20 MHz transducer changes in oxygen saturation within a single B-scan during occlusion have been shown [16]. Yet, all efforts to calculate 3D absorption maps of oxygen saturation, and melanin of the human skin *in vivo* have been unsuccessful. Moreover, it has recently been shown that the visualization of fine structures in the *stratum corneum*, and dermal papillae relies on the detection of ultrasonic frequencies above 60 MHz [17, 18].

Most recently, we have shown the first three-dimensional (3D) multispectral images of human skin, providing fully co-registered 3D absorption maps of melanin, oxyhemoglobin and deoxyhemoglobin [19]. In this work, we focus on the technical details and system design required in multispectral imaging of human skin. The MSOM system presented in this work achieves a lateral resolution of $<60\ \mu\text{m}$, and an axial resolution of $<13\ \mu\text{m}$ independent of wavelength.

2. MATERIALS AND METHODS

2.1 Experimental setup

The experimental setup was based on the recently developed RSOM system [20, 21]. A broadband spherically focused transducer with central frequency of $\sim 50\ \text{MHz}$, relative bandwidth of 100%, active element size of 3 mm, and an f number of ~ 1 was employed. The acoustic data was amplified by a 63dB low noise amplifier (63 dB, AU-1291, MITEQ Inc., Hauppauge, New York, USA), and recorded by a high-speed digitizer operated at a sampling rate of 500 MHz (CS122G1, Gage, Lockport, Illinois, USA). The tissue was excited by a flash-lamp pumped YAG/OPO (SpitLight 600 OPO, InnoLas Laser GmbH, Krailling, Germany) emitting 4-7 ns pulses in the spectral range from 413-680 nm with a repetition rate of 50 Hz. The laser was operated in wavelength-sweep mode emitting consecutive pulses at 530 nm, 540 nm, 550 nm, and 560 nm. The laser light was delivered to the tissue surface by a bifurcating fiber bundle, the core of each arm measuring 5 mm in diameter. The two fiber arms were positioned on both sides of the acoustic detector at an angle of approximately 60° with respect to the tissue surface in order to direct the light beams to the focal region of the detector. The illuminated area on the tissue surface measured approximately $50\ \text{mm}^2$ and the laser energy was below $700\ \mu\text{J}$ per pulse. Thus, both the ANSI laser safety limit of $20\ \text{mJ}/\text{cm}^2$ for single pulses and the limit of $2000\ \mu\text{W}/\text{mm}^2$ for repetitive pulsing were met [22].

The imaging head consisting of the transducer and the two fiber arms was attached to two motorized piezo stages (Physik Instrumente GmbH & Co. KG, Karlsruhe, Germany). The imaging head was raster-scanned with a step size of $10\ \mu\text{m}$ along the fast moving axis and $40\ \mu\text{m}$ along the slow moving axis. Since 4 different wavelengths were recorded successively, the acquisition step size for single wavelength data was $40\ \mu\text{m}$. A scan of a $5\ \text{mm} \times 3\ \text{mm}$ big area took approximately 13 minutes.

To couple the optoacoustic system to human skin, an interface unit (IU) consisting of acrylic glass with a $2\ \text{cm} \times 2\ \text{cm}$ opening was used. The opening of the IU, described in detail in [18], was sealed by applying slight pressure between the IU and the skin. The IU itself was filled with water. The light-transducer unit was held by an articulated arm and positioned on top of the IU, allowing to raster-scan the transducer through the opening of the IU.

2.2 Data processing

Originating from the slow repetition rate of the laser, we chose to under-sample data acquisition. To correct for spatial under-sampling, artificial views were calculated by linear interpolation of the measured data for positions in-between. The interpolation grid had a grid-size of $20\ \mu\text{m}$ and satisfied the Nyquist criteria for spatial sampling, stating that the acquisition step size should be smaller than half the lateral resolution of the system.

2.3 Reconstruction, and unmixing of chromophores

Image reconstruction was done with a 3D beam-forming algorithm similar to the reconstruction method described in [20, 21]. The beam-forming algorithm has been accelerated by parallelized computing on a GPU, and improved by incorporating the spatial sensitivity field of the detector as a weighting factor into the algorithm [19, 23]. The voxel size of the reconstruction grid was chosen to be 20 μm x 20 μm x 6 μm . Each single wavelength image was reconstructed separately. Due to the operation of the laser in wavelength-sweep mode the acquired multispectral data was inherently co-registered. The volumetric multispectral reconstructions were unmixed by a linear regression algorithm [1] with non-negative constraint considering the spectra of melanin, oxyhemoglobin, and deoxyhemoglobin.

2.4 Justification of high frequency transducer

The finite pulse width of the laser acts as a low pass filter. The larger the pulse width, the lower is the cutoff frequency of the low pass filter. In the previous single-wavelength implementation of the RSOM system [20, 21] a laser with a pulse width of <1 ns has been utilized, whereas the wavelength-tunable MSOM system utilizes a laser with 4-7 ns pulse width. The question arises if the laser source of the MSOM system is appropriate for the bandwidth of the 50 MHz transducer. To justify the appropriateness of our laser source we theoretically studied the signal distortion of a 15 μm thick solid suture made of nylon. The theoretical optoacoustic signal of the nylon suture was taken from [24]. To model bandpass filtering we digitally filtered the theoretical time signal by the bandpass data specified by the manufacturer. The laser pulse was modeled by a Gaussian curve with a FWHM of 7 ns, and the time signal was convoluted with the kernel function:

$$\text{kernel}(t) = e^{-\frac{4 \ln(2)t^2}{\text{FWHM}^2}} \quad (1)$$

Taking the Fourier Transform of the pulse width kernel function we obtain a low pass filter in frequency domain of the form:

$$\mathcal{F}_t \left[e^{-\frac{4 \ln(2)t^2}{\text{FWHM}^2}} \right] (f) \propto e^{-\frac{\pi^2 \text{FWHM}^2 f^2}{4 \ln(2)}} \quad (2)$$

2.5 System characterization

A phantom containing two sutures $\sim 15 \mu\text{m}$ in diameter (NYL03DS, vetsuture, France), and arranged to form a cross was used for the characterization of the system. The sutures were attached between two posts clued to a Petridish and immersed in water. The phantom was imaged by the same acquisition, data processing, and reconstruction protocol as for *in vivo* tissue. The lateral resolution was calculated from the mean lateral FWHM of the reconstructed sutures while taking into account the diameter d of the suture itself:

$$\text{lateral resolution} = \sqrt{\text{FWHM}^2 - d^2} \quad (3)$$

Since the theoretically expected axial resolution is expected to be $\sim 15 \mu\text{m}$ [25], and, thus, of the same size as the dimension of the suture itself, we estimated the axial resolution to be smaller than the measured axial FWHM of the sutures.

2.6 *In vivo* measurements

Two regions were imaged, the first one located at the thenar, and the second one located at the lower arm of a human volunteer.

3. RESULTS

3.1 Justification of high frequency transducer

The finite pulse width of the laser acts as a low pass filter. The larger the pulse width, the lower is the cutoff frequency of the low pass filter, which might hinder the acquisition of optoacoustic frequencies within the transducer bandpass. To justify the appropriateness of our laser source with a laser pulse length of 4-7 ns pulse width, we studied the influence of the laser pulse length and the transducer bandwidth on a theoretical optoacoustic signal. Fig. 1 shows the distortion of the analytical optoacoustic time signal and the frequency spectrum, originating from a 15 μm thick nylon suture surrounded by water. The black curve in Fig. 1(A) corresponds to the original optoacoustic time signal. When imaged with a bandwidth limited detector, the original signal broadens in time, as can be seen by the blue-dashed line in Fig. 1(A). The influence of the laser pulse length on the bandpass filtered signal is shown by the red-dotted line in Fig. 1(A). A pulse length of 7 ns causes an additional broadening of the time signal and, thus, a loss of resolution. The effect of temporal broadening can be understood by looking at the frequency spectrum of the distorted signals, as shown in Fig. 1(B). The transducer's bandwidth, depicted by the green dot-dashed curve in Fig. 1(B), filters out the detectable frequencies, in this case by shifting the maximum of the original frequency spectrum to lower frequencies. The laser pulse width, depicted by the magenta dot-dashed curve in Fig. 1(B), acts as a low pass filter and further reduces the original frequency content. From Eq. (2) we deduce that a laser pulse width with a FWHM of 7 ns translates into a low pass filter with a -6 dB cutoff frequency at 63 MHz. Thus, despite the low pass filtering properties of the laser pulse width broadband optoacoustic detection of acoustic frequencies above 50 MHz are still detectable.

3.2 System characterization

We continued by characterizing the lateral resolution of the system for each wavelength. Fig. 2 shows a reconstruction of two $\sim 15 \mu\text{m}$ sutures crossing each other as well as an exemplary cross section through the sutures in lateral and axial direction for all wavelengths. From Fig. 2(C,D) we see that the lateral and axial profiles of the suture are independent of wavelength. The mean width averaged over the whole length of the two sutures is summarized in Table 1. From the mean width of the reconstructed sutures we calculated a lateral resolution of 50-60 μm for all wavelengths under consideration. Given the axial FWHM of the upper reconstructed suture, we estimated the axial resolution of the system to be $< 13 \mu\text{m}$.

Table 1. Mean axial and lateral FWHM of the two reconstructed sutures shown in Fig. 2 for all imaging wavelengths.

wavelength [nm]	Upper suture		Lower suture	
	axial FWHM [μm]	lateral FWHM [μm]	axial FWHM [μm]	lateral FWHM [μm]
530	12.4	59.8	13.2	63.1
540	12.2	52.3	13.1	56.3
550	12.4	59.2	13.1	62.7
560	12.2	52.3	13.1	56.0

3.3 Multispectral unmixing for chromophores in the human palm

To show the ability to distinguish different tissue chromophores with MSOM, we imaged at the thenar area of a human volunteer, depicted in Fig. 3(B). The unmixed absorption maps of melanin, oxyhemoglobin, and deoxyhemoglobin are visualized in Fig. 3 by the green, red, and blue RGB channel, respectively. Fig. 3(A) shows a sagittal view of the ROI that marks the skin layers visualized in Fig. 3(C-E). Fig. 3(C) shows the layer where the epidermal-dermal junction is located. In this layer clusters of oxy- and deoxyhemoglobin are seen following the shape of the epidermal ridges. The superficial horizontal plexus, depicted in Fig. 3(D), shows the microvascular network, which is characterized by high blood oxygenation values. The deep horizontal plexus, visualized in Fig. 3(D), is characterized by large vessels that contain mostly deoxyhemoglobin as well as oxyhemoglobin.

3.4 Multispectral unmixing for chromophores in the lower arm

A second ROI located on the lower arm of a human volunteer, was imaged to study the capabilities of the unmixing method. The unmixed absorption maps of melanin, oxyhemoglobin, and deoxyhemoglobin are visualized in Fig. 4 by the green, red, and blue RGB channel, respectively. The sagittal view of the ROI, depicted in Fig. 4(A), shows strong melanin signal from the upper layer, whereas (de)oxyhemoglobin is mostly detected below the melanin. Fig. 4(B) illustrates a MAP of the upper layer. The absorption map shows strong melanin signal originating from the epidermal layer. In the upper layer most of the detected signal carries the spectral signature of melanin. Fig. 4(C) shows the vessels deeper inside the dermis. The vessels appear mostly deoxygenated.

4. DISCUSSION AND CONCLUSION

In this work we present a multispectral optoacoustic mesoscopy (MSOM) system, which provides three-dimensional absorption maps of melanin, oxyhemoglobin and deoxyhemoglobin. The MSOM systems provides a lateral resolution of $<60 \mu\text{m}$, and an axial resolution of $<15 \mu\text{m}$ independent of excitation wavelength. We have studied the influence of the laser pulse width on the optoacoustic frequency spectrum. The laser pulse width of 7 ns (FWHM) acts like a low pass filter with a -6 dB cutoff frequency at 63 MHz. We observed stronger absorption of melanin within the top layer of hairy skin located at the lower arm compared to glabrous skin at the thenar, which conforms to findings in the literature. The palm of the hand has very few melanocytes [26, 27]. Thus, the lower arm contains much more melanin than the thenar area on the palm. For both hairy and glabrous skin, we observed strong absorption of deoxyhemoglobin and oxyhemoglobin in the epidermal-dermal junction, the superficial, as well as deep horizontal plexus.

The low PRF of the laser proved to be the greatest challenge in obtaining the first volumetric multispectral images of human skin. Herein, we have presented a combined acquisition and data processing method that allowed for the acquisition of a 5 mm x 3 mm ROI in less than 13 minutes. First, we were able to remove reconstruction artifacts due to spatial under-sampling in the acquisition by the interpolation of missing data points from the acquired data itself. Second, the interleaved multispectral laser pulses allowed for intrinsic co-registration of multispectral datasets.

In a previous study it has been shown that single-wavelength RSOM pushes the limit of optical imaging in tumor angiogenesis [28]. MSOM will bring a new dimension to dermatology by its ability to quantify blood oxygenation levels, potentially visualizing metabolic alterations in skin cancer [29, 30].

5. ACKNOWLEDGEMENTS

Andreas Buehler and Vasilis Ntziachristos acknowledge funding from the European Union project FAMOS (FP7 ICT, contract no. 317744). Juan Aguirre acknowledges funding from the European Marie Curie IEF fellowships, project HIFI.

6. FIGURES

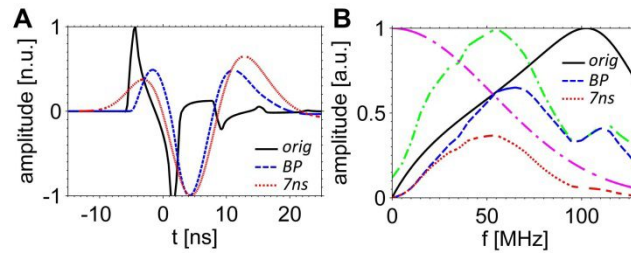


Figure 1. Impact of the transducer bandpass and the laser pulse width on a theoretical optoacoustic signal. A) Effect of bandpass and pulse width on a time signal originating from a 15 μm thick nylon suture surrounded by water. Solid black curve: analytic optoacoustic signal. Dashed blue curve: Bandpass filtered optoacoustic signal. Dotted red curve: Optoacoustic time signal that was bandpass filtered and convolved with a Gaussian curve corresponding to the laser pulse width. B) Frequency content of the optoacoustic signal. Solid black, dashed blue, and dotted red curve: Frequency content corresponding to the optoacoustic signals shown in (A). Dot-dashed green curve: Transducer bandpass as stated by the manufacturer. Dot-dashed magenta curve: Lowpass filter due to a 7 ns long laser pulse width.

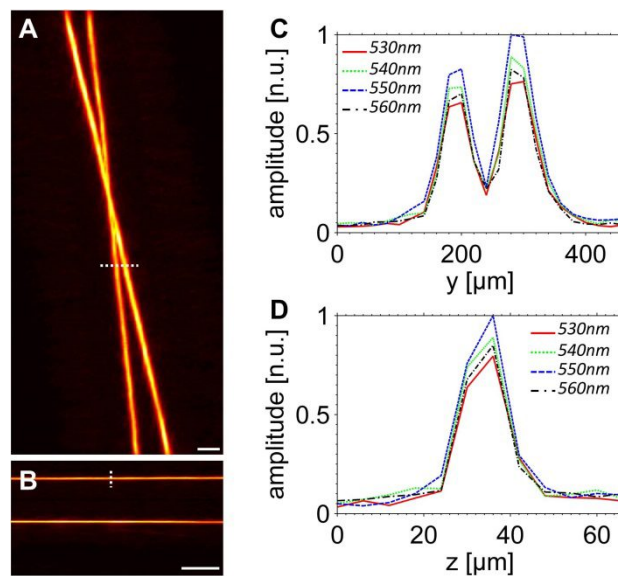


Figure 2. Lateral and axial profile of $\sim 15 \mu\text{m}$ thick sutures. A) Top-view of the suture phantom: MAP along the depth direction. The white dashed line corresponds to the location of the lateral profile shown in (C). B) Sagittal view of the suture phantom: MAP along the fast scanning direction. The white dashed line corresponds to the location of the axial profile shown in (D). C) Lateral profile of the two sutures at different wavelengths. D) Axial profile of the upper suture at different wavelengths. All scale bars: 250 μm

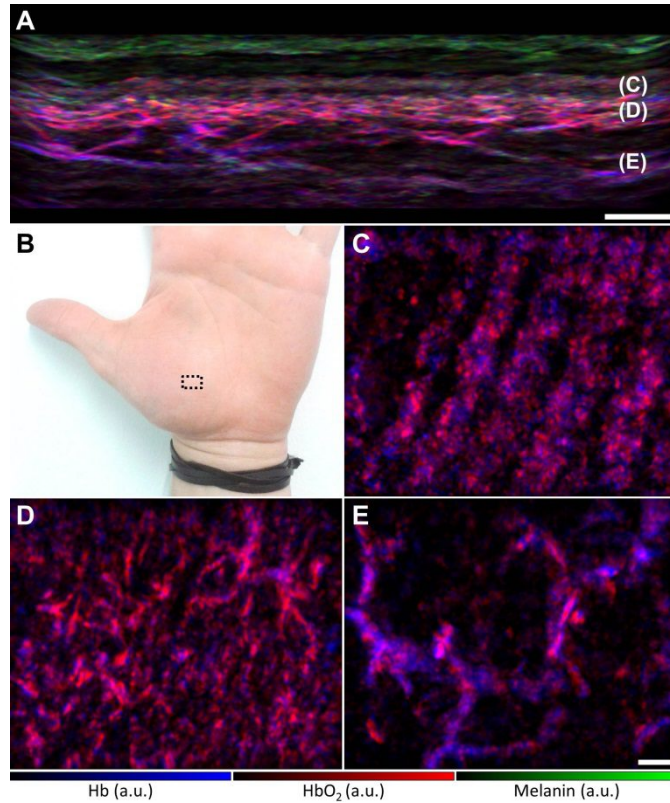


Figure 3. 3D unmixed images of the thenar area. In green, red, and blue the unmixing results for melanin, oxyhemoglobin, and deoxyhemoglobin, are shown, respectively. A) Side-view (Sagittal MAP) of the ROI shown in (B). B) Region of interest located on the human palm marked by the black dashed box. C) Coronal MAP of the dermal papillae layer. D) Coronal MAP of the superficial horizontal plexus. E) Coronal MAP of the deep horizontal plexus. All scale bars: 500 μm .

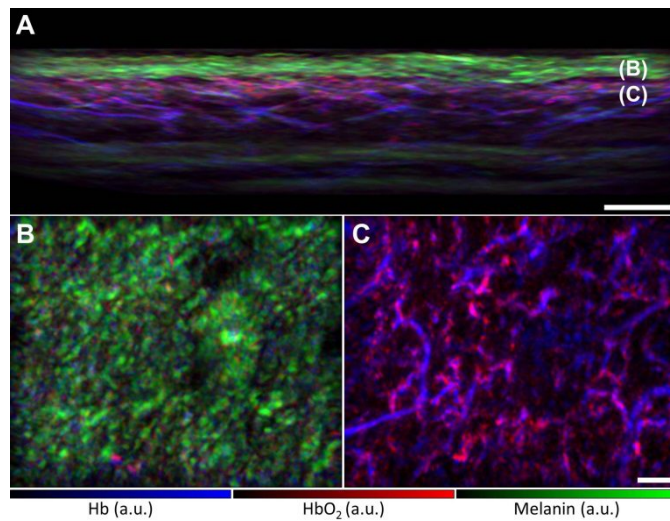


Figure 4. 3D unmixed images of the lower arm area. In green, red, and blue the unmixing results for melanin, oxyhemoglobin, and deoxyhemoglobin, are shown, respectively. A) Side-view (Sagittal MAP) of the ROI. B) Coronal MAP of the epidermal layer. C) Coronal MAP of the superficial horizontal plexus. All scale bars: 500 μm .

7. REFERENCES

- [1] Ntziachristos, V., and Razansky, D., "Molecular imaging by means of multispectral optoacoustic tomography (MSOT)," *Chem Rev*, 110(5), 2783-94 (2010).
- [2] Buehler, A., Kacprowicz, M., Taruttis, A., and Ntziachristos, V., "Real-time handheld multispectral optoacoustic imaging," *Opt Lett*, 38(9), 1404-6 (2013).
- [3] Dean-Ben, X. L., and Razansky, D., "Adding fifth dimension to optoacoustic imaging: volumetric time-resolved spectrally enriched tomography," *Light-Science & Applications*, 3, (2014).
- [4] Herzog, E., Taruttis, A., Beziere, N., Lutich, A. A., Razansky, D., and Ntziachristos, V., "Optical imaging of cancer heterogeneity with multispectral optoacoustic tomography," *Radiology*, 263(2), 461-8 (2012).
- [5] Buehler, A., Herzog, E., Razansky, D., and Ntziachristos, V., "Video rate optoacoustic tomography of mouse kidney perfusion," *Opt Lett*, 35(14), 2475-7 (2010).
- [6] Krishnaswamy, A., and Baranoski, G. V., [A study on skin optics] Tech. Rep. CS-2004-01, School of Computer Science, University of Waterloo, Canada, (2004).
- [7] Jacques, S. L., "Optical properties of biological tissues: a review," *Phys Med Biol*, 58(11), R37-61 (2013).
- [8] Lister, T., Wright, P. A., and Chappell, P. H., "Optical properties of human skin," *J Biomed Opt*, 17(9), 90901-1 (2012).
- [9] Bashkatov, A. N., Genina, E. A., and Tuchin, V. V., "Optical Properties of Skin, Subcutaneous, and Muscle Tissues: A Review," *Journal of Innovative Optical Health Sciences*, 4(1), 9-38 (2011).
- [10] Melillo, G., [Hypoxia and Cancer: Biological Implications and Therapeutic Opportunities] Springer Science & Business Media, (2013).
- [11] Brown, J. M., "Tumor hypoxia in cancer therapy," *Methods Enzymol*, 435, 297-321 (2007).
- [12] Steunou, A. L., Ducoux-Petit, M., Lazar, I., Monsarrat, B., Erard, M., Muller, C., Clottes, E., Burlet-Schiltz, O., and Nieto, L., "Identification of the hypoxia-inducible factor 2alpha nuclear interactome in melanoma cells reveals master proteins involved in melanoma development," *Mol Cell Proteomics*, 12(3), 736-48 (2013).
- [13] Silverstein, J. L., Steen, V. D., Medsger, T. A., and Falanga, V., "Cutaneous hypoxia in patients with systemic sclerosis (scleroderma)," *Archives of dermatology*, 124(9), 1379-1382 (1988).
- [14] Modarressi, A., Pietramaggiore, G., Godbout, C., Vigato, E., Pittet, B., and Hinz, B., "Hypoxia impairs skin myofibroblast differentiation and function," *J Invest Dermatol*, 130(12), 2818-27 (2010).
- [15] Zhang, H. F., Maslov, K., Stoica, G., and Wang, L. V., "Functional photoacoustic microscopy for high-resolution and noninvasive in vivo imaging," *Nat Biotechnol*, 24(7), 848-51 (2006).
- [16] Favazza, C. P., Cornelius, L. A., and Wang, L. V., "In vivo functional photoacoustic microscopy of cutaneous microvasculature in human skin," *J Biomed Opt*, 16(2), 026004 (2011).
- [17] Aguirre, J., Schwarz, M., Soliman, D., Buehler, A., Omar, M., and Ntziachristos, V., "Broadband mesoscopic optoacoustic tomography reveals skin layers," *Optics Letters*, 39(21), 6297 (2014).
- [18] Schwarz, M., Omar, M., Buehler, A., Aguirre, J., and Ntziachristos, V., "Implications of Ultrasound Frequency in Optoacoustic Mesoscopy of the Skin," *IEEE Trans Med Imaging*, 34(2), 672-677 (2014).
- [19] Schwarz, M., Buehler, A., Aguirre, J., and Ntziachristos, V., "Three-dimensional multispectral optoacoustic mesoscopy reveals melanin and blood oxygenation in human skin in vivo," *J Biophotonics*, (2015).
- [20] Omar, M., Gateau, J., and Ntziachristos, V., "Raster-scan optoacoustic mesoscopy in the 25-125 MHz range," *Opt Lett*, 38(14), 2472-4 (2013).
- [21] Omar, M., Soliman, D., Gateau, J., and Ntziachristos, V., "Ultrawideband reflection-mode optoacoustic mesoscopy," *Opt Lett*, 39(13), 3911-4 (2014).
- [22] American National Standards Institute, and The Laser Institute of America, [American National Standard for safe use of lasers : approved March 16, 2007] The Laser Institute of America, Orlando, FLa.(2007).
- [23] Turner, J., Estrada, H., Kneipp, M., and Razansky, D., "Improved optoacoustic microscopy through three-dimensional spatial impulse response synthetic aperture focusing technique," *Optics Letters*, 39(12), 3390-3393 (2014).
- [24] Khan, M. I., and Diebold, G. J., "The photoacoustic effect generated by laser irradiation of an isotropic solid cylinder," *Ultrasonics*, 34(1), 19-24 (1996).
- [25] Xu, M., and Wang, L. V., "Analytic explanation of spatial resolution related to bandwidth and detector aperture size in thermoacoustic or photoacoustic reconstruction," *Phys Rev E Stat Nonlin Soft Matter Phys*, 67(5 Pt 2), 056605 (2003).
- [26] Staricco, R. J., and Pinkus, H., "Quantitative and qualitative data on the pigment cells of adult human epidermis," *J Invest Dermatol*, 28(1), 33-45 (1957).

- [27] Szabo, G., "The number of melanocytes in human epidermis," *Br Med J*, 1(4869), 1016-7 (1954).
- [28] Omar, M., Schwarz, M., Soliman, D., Symvoulidis, P., and Ntziachristos, V., "Pushing the Optical Imaging Limits of Cancer with Multi-Frequency-Band Raster-Scan Optoacoustic Mesoscopy (RSOM)," *Neoplasia*, 17(2), 208-14 (2015).
- [29] Seyfried, T. N., Flores, R. E., Poff, A. M., and D'Agostino, D. P., "Cancer as a metabolic disease: implications for novel therapeutics," *Carcinogenesis*, 35(3), 515-527 (2014).
- [30] Seyfried, T. N., and Shelton, L. M., "Cancer as a metabolic disease," *Nutrition & Metabolism*, 7(7), 269-270 (2010).